Journal of Alloys and Compounds 937 (2023) 168465

Contents lists available at ScienceDirect

Journal of Alloys and Compounds

journal homepage: www.elsevier.com/locate/jalcom

Research Article

Effect of B2 ordering on the tensile mechanical properties of refractory $Al_xNb_{40}Ti_{40}V_{20-x}$ medium-entropy alloys

N. Yurchenko *, E. Panina, A. Tojibaev, V. Novikov, G. Salishchev, S. Zherebtsov, N. Stepanov

Belgorod National Research University, Belgorod 308015, Russia

A R T I C L E I N F O

Article history:
Received 31 October 2022
Received in revised form 25 November 2022
Accepted 12 December 2022
Available online 13 December 2022

Keywords:
Refractory high/medium-entropy alloys
B2 structure
Tensile tests
Mechanical properties
Portevin-Le Chatelier effect
Dynamic recrystallisation

A B S T R A C T

Most of refractory high/medium-entropy alloys show promising compressive mechanical properties at elevated temperatures. However, scarce tensile testing data hinder the estimation of the applicability of these alloys for potential high-temperature service. It is also unclear how an ordered structure, which improves high-temperature compressive strength, will affect the tensile performance. This work demonstrated that the effect of B2 ordering on the tensile mechanical properties of new refractory $Al_xNb_{40}Ti_{40}V_{20-x}$ (x = 0; 15; 20 at%) medium-entropy alloys was manifold, and it depended on the chemical composition. In an $Al_{15}Nb_{40}Ti_{40}V_5$ alloy having a weak degree of B2 ordering, large uniform room-temperature elongation and moderate high-temperature strength, comparable with a bcc $Nb_{40}Ti_{40}V_{20}$ alloy, were found. An $Al_{20}Nb_{40}Ti_{40}$ alloy with the high degree of B2 ordering was brittle at room-temperature and sensitive to testing environment at elevated temperatures. Meantime, it softened notably slower up to 0.4 T_m, albeit losing strength at > 0.4 T_m faster than the bcc $Nb_{40}Ti_{40}V_{20}$ or weakly B2-ordered $Al_{15}Nb_{40}Ti_{40}V_5$ alloys. Factors responsible for the resulted mechanical properties were thoroughly discussed.

1. Introduction

The refractory high/medium-entropy (RH/MEAs) concept revived fading interest in refractory alloys as structural materials for high-temperature applications [1–4]. Up to date, numerous RH/MEAs with excellent strength [5–9] and oxidation resistance [10,11], as well as with decent thermal stability [12–14], were designed. Still, such an essential property for practical usage, like tensile ductility, remains achievable only for a very limited set of RH/MEAs developed [15].

Most of RH/MEAs having tensile ductility belong to a Hf-Ta-Nb-Ti-V-Zr system and its derivates [15–21]. These alloys usually possess a single-phase body-centred cubic (bcc) structure, in which plastic deformation is mediated by a glide of $\frac{a}{2}<111>$ screw dislocations [19,22]. Existing literature data suggest that phase transformations [23–26] (except for transformation-induced plasticity (TRIP) [27–29]), coarse secondary particles [30,31], or B2 ordering [32] should be avoided/suppressed to maintain reasonable elongation in RH/MEAs.

Meantime, recent studies on Ti-rich H/MEAs reported that weak B2 ordering was not harmful to ambient tensile ductility [33–35]. Our late work demonstrated that the same held true for a NbTiZr RMEA [36]. Specifically, we showed that controllable Al-induced B2 ordering helped overcome the strength-ductility trade-off at room temperature. The improvement of properties originated from solid solution and short-range order strengthening, coupled with changing of dislocation glide character [36]. Thus, it seems highly intriguing to investigate the effect of Al-induced B2 ordering on the tensile performance of RH/MEAs further. Moreover, a wider temperature interval should be explored, because, despite being positioned as potential substitutes for existing high-temperature alloys, RH/MEAs have been subjected to tensile tests at elevated temperatures extremely rare [37–40].

This study delivers a comprehensive analysis of the influence of Al-induced B2 ordering on the room- and high-temperature tensile mechanical properties of new RMEAs. As a starting alloy, we chose a non-equiatomic $Nb_{40}Ti_{40}V_{20}$ (at%) RMEA, since its equiatomic NbTiV counterpart with the bcc structure showed good strength-ductility synergy at room temperature [41]. To provoke the possible B2 ordering in the $Nb_{40}Ti_{40}V_{20}$ alloy, vanadium was replaced by certain amounts of Al.

* Corresponding author.
E-mail address: yurchenko_nikita@bsu.edu.ru (N. Yurchenko).

https://doi.org/10.1016/j.jallcom.2022.168465
0925-8388/

Table 1
Actual chemical compositions and melting points, T_m, of the $Al_xNb_{40}Ti_{40}V_{20-x}$ alloys. Concentrations of constitutive elements (metals) were measured by energy-dispersive X-ray spectroscopy (EDS; FEI Quanta 600 FEG); the content of impurities (oxygen and nitrogen) was determined by inert gas fusion (Meteck-300/600 (GRANAT, Russia, Saint Petersburg). Melting points were obtained by thermodynamic modeling using Thermo-Calc software with a specialised database for high-entropy alloys (TCHEA 4.0) (Thermo-Calc Software, Solna, Sweden).

Alloy	Chemical composition, at%				O, ppm	N, ppm	T_m, °C
	Al	Nb	Ti	V			
$Nb_{40}Ti_{40}V_{20}$	–	38.9 ± 0.4	38.9 ± 0.1	22.2 ± 0.1	450 ± 11	32 ± 8	1812
$Al_{15}Nb_{40}Ti_{40}V_5$	14.4 ± 0.3	38.9 ± 0.2	40.1 ± 0.1	6.6 ± 0.2	445 ± 6	30 ± 7	1705
$Al_{20}Nb_{40}Ti_{40}$	19.3 ± 0.2	40.4 ± 0.1	40.3 ± 0.3	–	448 ± 8	33 ± 9	1808

2. Materials and methods

The alloys with nominal compositions of $Nb_{40}Ti_{40}V_{20}$, $Al_{15}Nb_{40}Ti_{40}V_5$, and $Al_{20}Nb_{40}Ti_{40}$ (at%) were produced by the vacuum arc melting of pure metals (> 99.9 wt%). The as-cast ingots were subjected to a thermo-mechanical treatment included cold rolling to 80 % of thickness and subsequent annealing in a Nabertherm furnace at 1200 °C for 5 min ($Nb_{40}Ti_{40}V_{20}$), 1200 °C for 1 min ($Al_{20}Nb_{40}Ti_{40}$), and at 1050 °C for 15 min ($Al_{15}Nb_{40}Ti_{40}V_5$). Prior to annealing, the specimens were sealed in vacuumed (10^{-2} torr) tubes filled with titanium chips for prevent any oxidation.

For the evaluation of mechanical properties, tensile tests of the dog-bone specimens with the gauge dimensions of $6 \times 3 \times 1$ mm^3 were performed at 25, 500, 700, and 900 °C in the laboratory air at a constant strain rate of 10^{-3} s^{-1} using an Instron 5882 machine equipped with a radial furnace. The digital image correlation (DIC) technique was employed to visualise the distribution of local strains produced during the room-temperature tensile tests. The in-plane Lagrangian strains were measured using a commercial Vic-3D™ system (Correlated Solutions, Inc).

Microstructural investigations were performed using X-ray diffraction (XRD; RIGAKU diffractometer and Cu Kα radiation), electron backscatter diffraction (EBSD; FEI Quanta 600 FEG), energy dispersive spectroscopy (EDS; FEI Quanta 600 FEG), and transmission electron microscopy (TEM; JEM JEOL-2100). Selected area diffraction patterns (SADPs) were collected in $< 001 >_{bcc}$ zone axes at an exposure time of 16 s. Intensity line profiles along the g_{200} vector were constructed using ImageJ [36]. Data on the actual chemical composition of the alloys are given in Table 1.

3. Results and discussion

3.1. Initial structure

Fig. 1 displays data on the phase composition and microstructure of the $Al_xNb_{40}Ti_{40}V_{20-x}$ alloys. According to XRD charts, all three alloys had a single-phase bcc structure (Fig. 1a). The Al alloying shifted Bragg's peaks to smaller 2θ values, indicating a gradual increase in the lattice parameter. The latter enlarged from 0.3239 ± 0.0001 nm in the $Nb_{40}Ti_{40}V_{20}$ alloy to 0.3258 ± 0.0001 nm in the $Al_{20}Nb_{40}Ti_{40}$ alloy. Inverse pole figure (IPF) maps, collected during EBSD analysis, showed that all the alloys had fully recrystallised microstructures with close average grain sizes measured as ~ 30–35 µm (Fig. 1b-d). SEM-EDS maps illustrated relatively homogeneous distributions of constitutive elements in the alloys studied (Fig. S1, Supplementary material).

Bearing in mind the low capability of conventional XRD analysis to reveal the B2 ordering in RH/MEAs even with high Al content [42,43], we applied TEM technique for a more robust structure

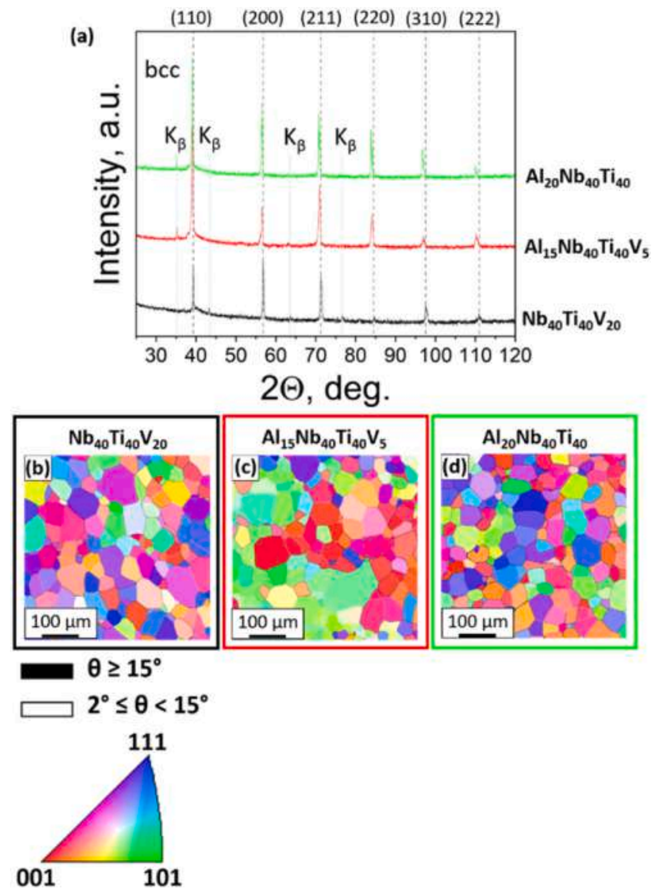

Fig. 1. Characterisation of the structure of the $Al_xNb_{40}Ti_{40}V_{20-x}$ alloys: (a) XRD charts, showing the single-phase bcc structure in all the studied alloys; (b-d) IPF maps, illustrating the fully recrystallised microstructure formed in the $Nb_{40}Ti_{40}V_{20}$ (b), $Al_{15}Nb_{40}Ti_{40}V_5$ (c), and $Al_{20}Nb_{40}Ti_{40}$ (d) alloys.

characterisation of the $Al_xNb_{40}Ti_{40}V_{20-x}$ alloys. Bright-field imaging (Fig. 2a) and SADP taken in the $[001]_{bcc}$ zone axis (Fig. 2b), which was further examined via the intensity profile line along g_{200} (Fig. 2c), confirmed the single-phase bcc structure of the $Nb_{40}Ti_{40}V_{20}$ alloy. The same analysis performed for the $Al_{15}Nb_{40}Ti_{40}V_5$ and $Al_{20}Nb_{40}Ti_{40}$ alloys (Fig. 2d-i) revealed {100} superlattice spots in SADPs with an intensity and width, which increased from the $Al_{15}Nb_{40}Ti_{40}V_5$ to the $Al_{20}Nb_{40}Ti_{40}$ alloy. Dark-field imaging of both alloys (Fig. 2d, g) under the {100} superlattice spots disclosed the structural entities similar to the irregular-shaped B2 domains (bright regions) separated by antiphase boundaries (APBs; dark interlayers). The size of the B2 domains in the $Al_{15}Nb_{40}Ti_{40}V_5$ alloy was ~ 30 nm,

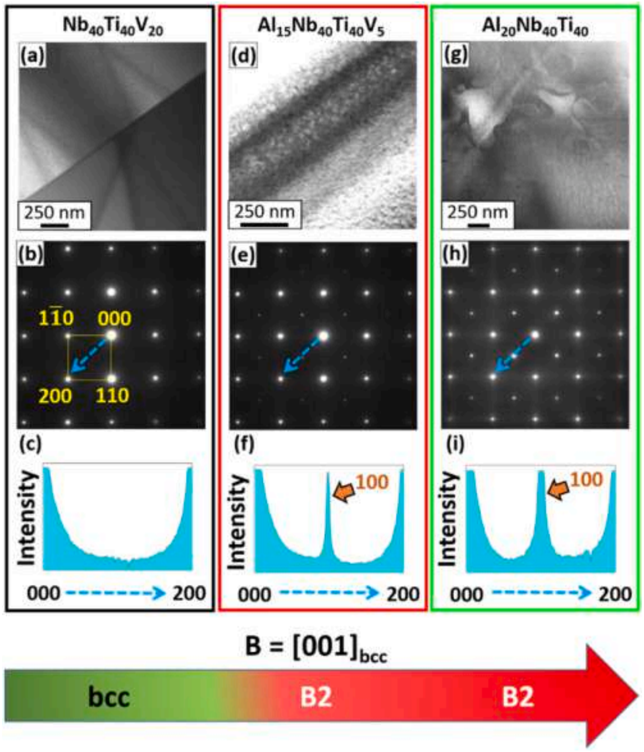

Fig. 2. Detailed characterisation of the structure of the $Al_xNb_{40}Ti_{40}V_{20-x}$ alloys: (a-c) TEM image (a), showing typical structure, SADP (b), acquired in $[001]_{bcc}$ zone axis, intensity line profile along the g_{200} vector (c) (the direction is denoted with dashed blue arrows in SADP ((b) of the $Nb_{40}Ti_{40}V_{20}$ alloy; (d-f) TEM image (d), showing typical structure, SADP (f), acquired in $[001]_{bcc}$ zone axis, intensity line profile along the g_{200} vector (f) (the direction is denoted with dashed blue arrows in SADP (e) of the $Al_{15}Nb_{40}Ti_{40}V_5$ alloy; (g-i) TEM image (g), showing typical structure, SADP (h), acquired in $[001]_{bcc}$ zone axis, intensity line profile along the g_{200} vector (i) (the direction is denoted with dashed blue arrows in SADP (h) of the $Al_{20}Nb_{40}Ti_{40}$ alloy. (d, g) acquired in dark-field modes under (100) superlattice spots, visible in (e, h), displaying the presence of B2 domains (bright irregular-shaped areas) and APBs (dark interlayers); Orange arrows in (f, i) denoted the peaks, corresponded to the {100} local maxima in the $Al_{15}Nb_{40}Ti_{40}V_5$ (f) and $Al_{20}Nb_{40}Ti_{40}$ (i) alloys.

while, in the $Al_{20}Nb_{40}Ti_{40}$ alloy, it varied from ~ 100 to ~ 700 nm. These observations can support previous suggestions [36,44] about the operation of domain ordering mechanism in B2-ordered RH/MEAs, according to which the larger the dimensions of the B2 domains due to the increasing Al content, the higher the degree of B2 ordering. However, the substitution of constitutive elements with Al in a B2 sublattice seems to be another reason for the enlarged intensity of the {100} superlattice spots and, thus, the degree of B2 ordering [43,45,46]. Therefore, the more intensive and thicker {100} superlattice spots, along with the larger B2 domains, in the $Al_{20}Nb_{40}Ti_{40}$ alloy compared to those in the $Al_{15}Nb_{40}Ti_{40}V_5$ alloy could hint at a higher degree of B2 ordering. Based on this qualitative analysis, we classified the $Al_{15}Nb_{40}Ti_{40}V_5$ and $Al_{20}Nb_{40}Ti_{40}$ alloys as weakly and highly B2-ordered, respectively.

3.2. Mechanical properties

3.2.1. Room-temperature

Fig. 3 and Table 2 collect the room-temperature mechanical properties and fractography data of the $Al_xNb_{40}Ti_{40}V_{20-x}$ alloys. The bcc $Nb_{40}Ti_{40}V_{20}$ alloy showed the lowest (650 MPa) yield strength, *YS*, among the studied alloys. The weakly B2-ordered $Al_{15}Nb_{40}Ti_{40}V_5$ alloy demonstrated moderate *YS* of 750 MPa, while *YS* of highly B2-ordered $Al_{20}Nb_{40}Ti_{40}$ alloy was only slightly higher (795 MPa) (Fig. 3a; Table 2).

A more pronounced effect of the Al alloying should be noted for ductility. Both ternary bcc $Nb_{40}Ti_{40}V_{20}$ and highly B2-ordered $Al_{20}Nb_{40}Ti_{40}$ alloys manifested rather an expected behaviour for these structures: the bcc alloy was ductile, while its B2-ordered counterpart stood as brittle (Fig. 3a, Table 2). In turn, the weakly B2-ordered $Al_{15}Nb_{40}Ti_{40}V_5$ alloy showed a 22 % higher elongation at fracture, *EF*, compared to the arbitrary bcc $Nb_{40}Ti_{40}V_{20}$ alloy. Fractographic examination revealed multiple dimples in the $Nb_{40}Ti_{40}V_{20}$ and $Al_{15}Nb_{40}Ti_{40}V_5$ alloys, but intergranular fracture in the $Al_{20}Nb_{40}Ti_{40}$ alloy (Fig. 3b-d).

Another interesting aspect was the difference in post-yielding behaviour of the bcc $Nb_{40}Ti_{40}V_{20}$ and weakly B2-ordered $Al_{15}Nb_{40}Ti_{40}V_5$ alloys. According to engineering stress-strain curves, the bcc $Nb_{40}Ti_{40}V_{20}$ alloy demonstrated strengthening until ~ 12 % of strain, attaining the ultimate tensile strength, *UTS*, of 700 MPa. Meantime, the weakly B2-ordered $Al_{15}Nb_{40}Ti_{40}V_5$ alloy showed a significantly shorter strengthening stage (up to ~ 0.4 %) before achieving the *UTS* of 775 MPa, which was further followed by gradual softening until ~ 10 % of strain, then changed to continuous yielding.

Similar plateau-like engineering stress-strain curves were previously found in numerous bcc and weakly B2-ordered (R)H/MEAs [17,33,34,36,47,48]. Such behaviour could indicate the occurrence of the instability of plastic flow after yielding, resulting in a rapid localisation of plastic deformation. However, recent studies, in which DIC technique was used, revealed no early necking for alloys demonstrating these types of curves [17,36]. Indeed, true strain-stress curves supported by DIC images of the tensile specimens showed that the weakly B2-ordered $Al_{15}Nb_{40}Ti_{40}V_5$ alloy with a “dropped-then-recovered” dependence of strain hardening rate, θ, [36] achieved a higher uniform elongation compared to the bcc $Nb_{40}Ti_{40}V_{20}$ counterpart having a “normal” decrease of θ with the evolving strain.

The resulted deformation behaviour of the $Al_{15}Nb_{40}Ti_{40}V_5$ alloy and its ductility improvement over the $Nb_{40}Ti_{40}V_{20}$ alloy could originate from changing of dislocation movement due to the Al-induced B2 ordering. EBSD analysis of the tested specimens showed a clear difference in the deformed structures of these alloys (Figs. 4 and S2, Supplementary materials). In the bcc $Nb_{40}Ti_{40}V_{20}$ alloy, highly localised macroscopic zones surrounded by multiple intact regions were observed (Fig. 4a-c). Inside the heavily deformed grains, misorientation profile revealed numerous kink bands [49,50] (Fig. 4c).

In turn, in the weakly B2-ordered $Al_{15}Nb_{40}Ti_{40}V_5$ alloy, the deformation-induced substructure was more homogeneous (Fig. 4d, e). Fine structure characterisation revealed profuse dislocation bands (DBs) (Fig. 4 f), which were formed by $\frac{a}{2}$ < 111 > screw dislocations because of local reduction of the degree of B2 ordering [36]. We infer that microscopic localisation of plastic deformation in DBs observed in the weakly B2-ordered $Al_{15}Nb_{40}Ti_{40}V_5$ alloy ensured a more stable plastic flow and, thus, higher *EF* compared to the bcc $Nb_{40}Ti_{40}V_{20}$ alloy, in which macroscopic localisation created additional stress concentrators, leading to the premature crack formation.

3.2.2. 500 °C

Fig. 5 and Table 3 assemble the mechanical properties of the $Al_xNb_{40}Ti_{40}V_{20-x}$ alloys tested at 500 °C. An increase in the testing

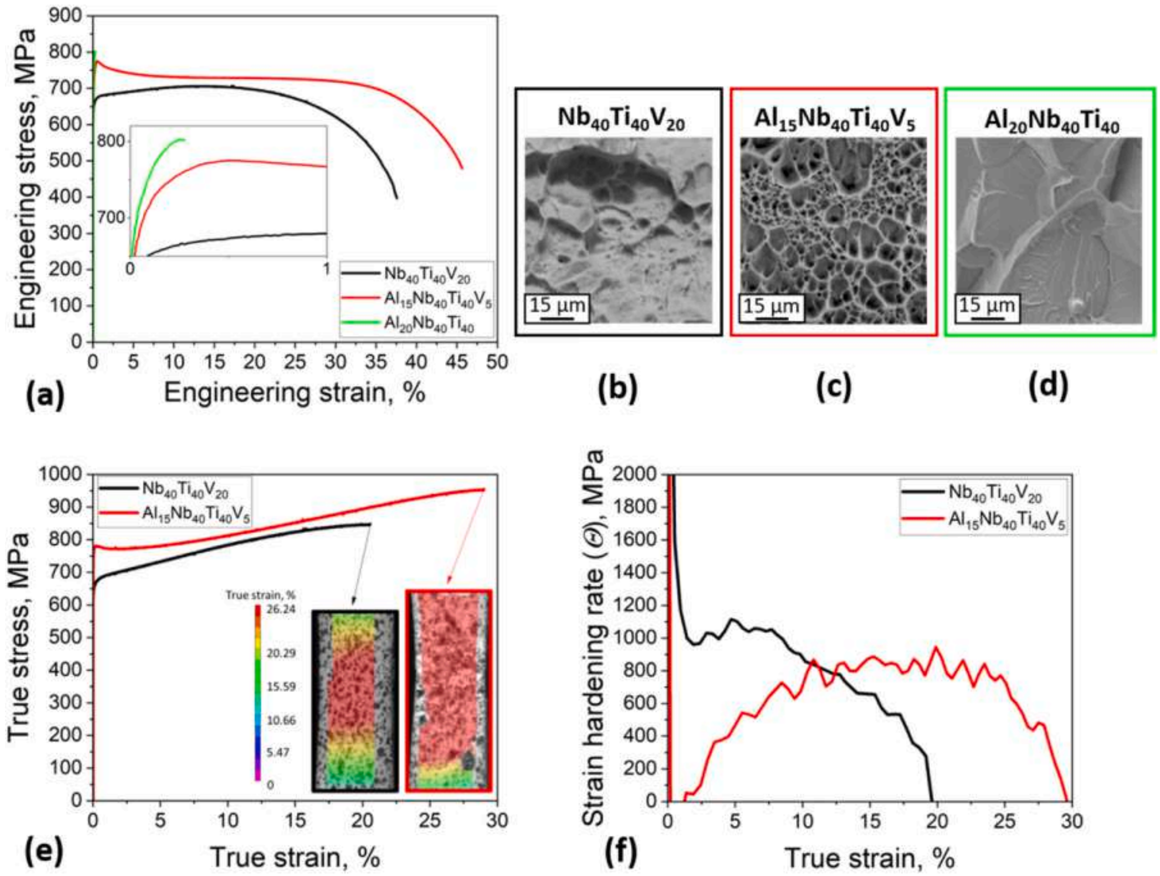

Fig. 3. Characterisation of room-temperature tensile mechanical properties of the $Al_xNb_{40}Ti_{40}V_{20-x}$ alloys: (a) engineering stress-strain curves with an enlarged insert, showing the low-strain region; (b-d) fracture surfaces of the $Nb_{40}Ti_{40}V_{20}$ (b), $Al_{15}Nb_{40}Ti_{40}V_5$ (c), and $Al_{20}Nb_{40}Ti_{40}$ (d) alloys; (e) true stress-strain curves of the $Nb_{40}Ti_{40}V_{20}$ and $Al_{15}Nb_{40}Ti_{40}V_5$ alloys with respective DIC images of tensile specimens, taken at the necking formation and demonstrating the strain distribution along the cross-section; (f) evolution of strain hardening rate, θ, with strain.

Table 2
Yield strength, *YS*, ultimate tensile strength, *UTS*, elongation at fracture, *EF*, and elastic moduli, *E*, obtained during room-temperature tensile tests of the $Al_xNb_{40}Ti_{40}V_{20-x}$ alloys. *E* were evaluated by DIC technique.

Alloy	*YS*, MPa	*UTS*, MPa	*EF*, %	*E*, GPa
$Nb_{40}Ti_{40}V_{20}$	650 ± 20	700 ± 15	37.2 ± 0.4	105.3 ± 2.5
$Al_{15}Nb_{40}Ti_{40}V_5$	750 ± 15	775 ± 10	45.6 ± 0.3	108.1 ± 1.7
$Al_{20}Nb_{40}Ti_{40}$	795 ± 25	800 ± 20	0.3 ± 0.1	93.2 ± 3.1

temperature resulted in the ~ 40 %-softening of the bcc $Nb_{40}Ti_{40}V_{20}$ and weakly B2-ordered $Al_{15}Nb_{40}Ti_{40}V_5$ alloys compared to room temperature, while retaining similar ductility (Tables 2 and 3). The strength degradation of the highly B2-ordered $Al_{20}Nb_{40}Ti_{40}$ alloy was less pronounced (27 %), but its *EF* increased notably (Fig. 5a; Table 3).

Besides the superiority in the strength over the bcc $Nb_{40}Ti_{40}V_{20}$ alloy, both B2-ordered alloys manifested Portevin-Le Chatelier (PLC) effect (Fig. 5b, c). We found that the amplitude and frequency of serrations were depended on the strain and Al content. In the $Al_{15}Nb_{40}Ti_{40}V_5$ alloy, the first stress drop was observed at < 5 % of strain, and its amplitude did not exceed ~ 1 MPa. Up to ~21 % of strain, the amplitude of serrations increased mildly, while it raised abruptly to ~20–25 MPa at > 21 % of strain. This amplitude remained almost constant up to 30–35 % of strain, decreasing in the post-necking region of the stress-strain curve. Starting from ~27 % of strain and until fracture, the frequency of serrations augmented.

Similar to the $Al_{15}Nb_{40}Ti_{40}V_5$ alloy, the serrations in the $Al_{20}Nb_{40}Ti_{40}$ alloy commenced at ~ 5 % of strain, but their amplitude was significantly larger (~25–30 MPa), and this value persisted until ~ 17 % of strain. The stress drops were occasional up to ~15 % of strain, while they became more regular with further straining.

The manifestation of PLC effect in RH/MEAs can be attributed to different reasons, of which interactions of dislocations with interstitial solutes appear to be the most frequent. Particularly, Eleti et al. [39] observed the PLC effect in the bcc NbTiZr RMEA during tensile testing at 200 °C, and connected it with the presence of C and/or O atoms. If the same mechanism had operated in the $Al_xNb_{40}Ti_{40}V_{20-x}$ RMEAs, even the bcc $Nb_{40}Ti_{40}V_{20}$ alloy would demonstrate the PLC effect, since the contamination by impurities was equal in all three alloys (Table 1). However, the PLC effect was exclusive for the B2-ordered alloys, indicating the other factors could induce this phenomenon.

Recently, Laube et al. [43] used the theoretical basis after Rong [51] and speculated that the PLC effect in the B2-ordered Al_x(MoTiCr)$_{100-x}$ RMEAs originated from the pinning and unpinning process of dislocations at APBs. Careful TEM analysis of the deformed fine

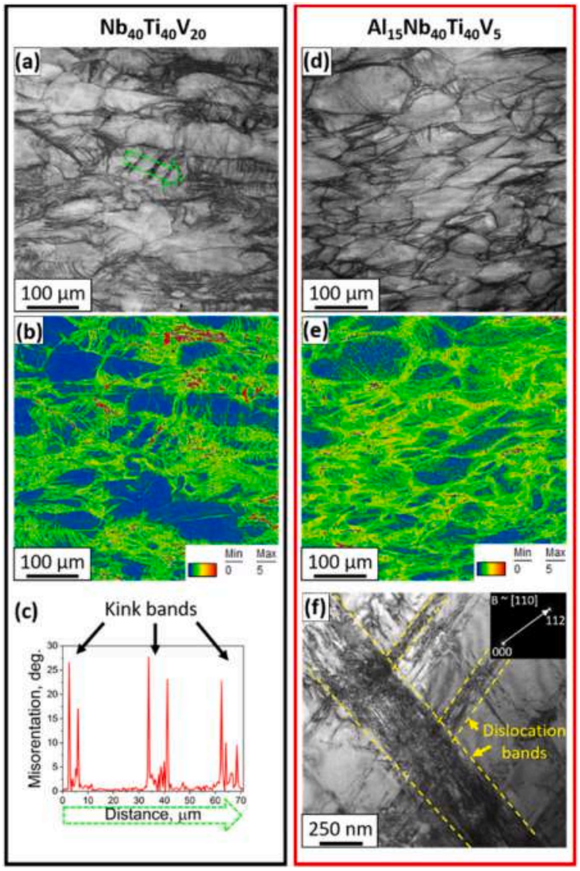

Fig. 4. Characterisation of the structure of the $Nb_{40}Ti_{40}V_{20}$ (a-c) and $Al_{15}Nb_{40}Ti_{40}V_5$ (d-f) alloys after room-temperature tensile tests: (a, d) Image Quality maps of the $Nb_{40}Ti_{40}V_{20}$ (a) and $Al_{15}Nb_{40}Ti_{40}V_5$ (d) alloys; (b, e) Kernel Average Misorientation maps of the $Nb_{40}Ti_{40}V_{20}$ (b) and $Al_{15}Nb_{40}Ti_{40}V_5$ (e) alloys; (c) misorientation profile taken from the line denoted with a dotted green arrow in Fig. 1a, confirming the presence of kink bands in the $Nb_{40}Ti_{40}V_{20}$ alloy; (f) TEM bright-field image of the fine structure with denoted $\vec{g}$ = 112 near $[110]_{B2}$ zone axis, showing profuse dislocation bands (DBs) in the $Al_{15}Nb_{40}Ti_{40}V_5$ alloy. The tensile direction is horizontal for a, b, d, e.

structure of the $Al_{15}Nb_{40}Ti_{40}V_5$ alloy both in bright-(Fig. 6a) and dark-field (Fig. 6b) regimes revealed that $\frac{a}{2} < 111 >$ screw dislocations were pinned on the boundaries of B2 domains, and also cut

Table 3
Yield strength, *YS*, ultimate tensile strength, *UTS*, elongation at fracture, *EF*, obtained during tensile tests of the $Al_xNb_{40}Ti_{40}V_{20-x}$ alloys at 500 °C.

Alloy	*YS*, MPa	*UTS*, MPa	*EF*, %
$Nb_{40}Ti_{40}V_{20}$	405 ± 25	525 ± 35	35.8 ± 0.6
$Al_{15}Nb_{40}Ti_{40}V_5$	470 ± 15	565 ± 20	45.1 ± 0.8
$Al_{20}Nb_{40}Ti_{40}$	580 ± 60	685 ± 10	21.7 ± 2.6

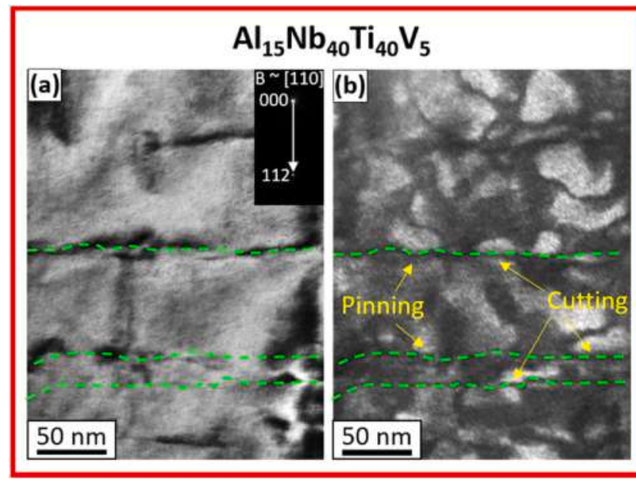

Fig. 6. Characterisation of the fine structure of the $Al_{15}Nb_{40}Ti_{40}V_5$ alloy after tensile test at 500 °C: bright- (a) and dark-field (b) TEM images with denoted $\vec{g}$ = 112 near $[110]_{B2}$ zone axis (a), showing the interactions of dislocations (marked with green dotted lines) with B2 domains.

these domains. This repeated process of trapping-detrapping of dislocations by B2 domains seems to be the most plausible explanation of the PLC effect in the B2-ordered $Al_{15}Nb_{40}Ti_{40}V_5$ and $Al_{20}Nb_{40}Ti_{40}$ alloys. Variations in the manifestation of the PLC effect between these two alloys could be connected with different B2 domain sizes (Fig. 2d, g) and, possibly, APBs energies. Meanwhile, the evolution of serrations with the strain seemed to be related to the increasing events of trapping-detrapping of dislocations by B2 domains. However, these statements should be verified further, which is beyond of the scope of the current study.

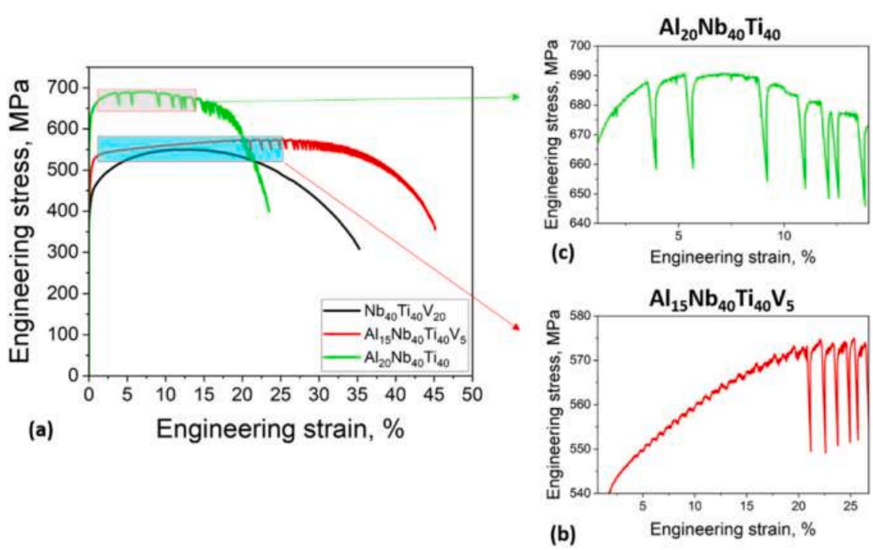

Fig. 5. Characterisation of tensile mechanical properties of the $Al_xNb_{40}Ti_{40}V_{20-x}$ alloys at 500 °C: (a) engineering stress-strain curves; (b, c) the enlarged regions of the stress-strain curves, showing the manifestation of PLC effect in the $Al_{15}Nb_{40}Ti_{40}V_5$ (b) and $Al_{20}Nb_{40}Ti_{40}$ (c) alloys.

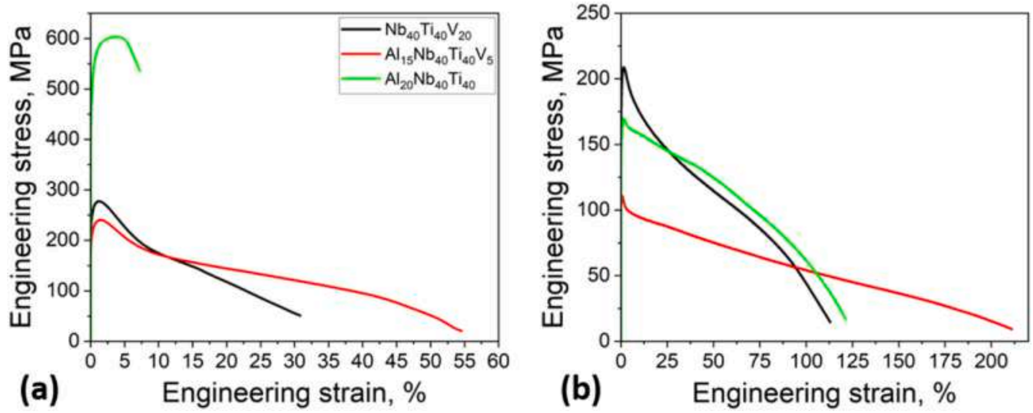

Fig. 7. Characterisation of tensile mechanical properties of the $Al_xNb_{40}Ti_{40}V_{20-x}$ alloys at 700 and 900 °C: engineering stress-strain curves obtained after tensile tests at 700 (a) and 900 °C (b).

Table 4
Yield strength, *YS*, ultimate tensile strength, *UTS*, elongation at fracture, *EF*, obtained during tensile tests of the $Al_xNb_{40}Ti_{40}V_{20-x}$ alloys at 700 and 900 °C.

Alloy	T = 700 °C		
	YS, MPa	*UTS*, MPa	*EF*, %
$Nb_{40}Ti_{40}V_{20}$	245 ± 15	275 ± 10	30.8 ± 1.6
$Al_{15}Nb_{40}Ti_{40}V_5$	210 ± 15	240 ± 15	54.6 ± 0.5
$Al_{20}Nb_{40}Ti_{40}$	510 ± 20	595 ± 20	6.3 ± 1.0
Alloy	T = 900 °C		
	YS, MPa	*UTS*, MPa	*EF*, %
$Nb_{40}Ti_{40}V_{20}$	180 ± 5	210 ± 5	120.5 ± 10.6
$Al_{15}Nb_{40}Ti_{40}V_5$	105 ± 5	110 ± 5	211.1 ± 3.6
$Al_{20}Nb_{40}Ti_{40}$	150 ± 10	170 ± 10	121.2 ± 2.2

3.2.3. 700 and 900 °C

Fig. 7 and Table 4 summarise the mechanical properties of the $Al_xNb_{40}Ti_{40}V_{20-x}$ alloys tested at 700 and 900 °C. At 700 °C, the weakly B2-ordered $Al_{15}Nb_{40}Ti_{40}V_5$ alloy softened drastically down to 210 MPa with a somewhat ductility increment, and it became slightly weaker than the bcc $Nb_{40}Ti_{40}V_{20}$ alloy (*YS* = 245 MPa), which *EF* decreased. The highly B2-ordered $Al_{20}Nb_{40}Ti_{40}$ alloy demonstrated more than twice higher strength (*YS* = 510 MPa), but the smallest value of *EF* (Fig. 7a; Table 4).

At 900 °C, both B2-ordered alloys had smaller *YS* (≤ 150 MPa) compared to the bcc $Nb_{40}Ti_{40}V_{20}$ (*YS* = 180 MPa) counterpart (Fig. 7b; Table 4). Meantime, the ductility of all three alloys increased substantially. Specifically, elongation of the bcc $Nb_{40}Ti_{40}V_{20}$ and highly B2-ordered $Al_{20}Nb_{40}Ti_{40}$ alloy was almost equal, reaching ~120 %. In turn, *EF* of the weakly B2-ordered $Al_{15}Nb_{40}Ti_{40}V_5$ alloy exceeded 200 %.

The strength breakdown at 700 and 900 °C, which were corresponded to 0.39–0.53 T_m (Table 1), could hint at the activation of diffusion-controlled dislocation climb/glide [52]. Wherein, the highly B2-ordered $Al_{20}Nb_{40}Ti_{40}$ alloy sustained to thermal softening better than the weakly B2-ordered $Al_{15}Nb_{40}Ti_{40}V_5$ alloy (Fig. 7a; Table 4). This superiority appeared to stem from the higher degree of B2 ordering (Fig. 2; Section 3.1), as it was previously reported by Yurchenko et al. [45] and Laube et al. [43]. In turn, the advantage of B2-ordered structure eliminated completely at 900 °C (Fig. 7b; Table 4). The most probable reason for such a steep strength drop was the reduction of the degree of B2 ordering or even disordering [53].

The similarity in the deformation behaviour of the alloys studied should also be noted. A close look at stress-strain curves revealed that, after yielding both at 700 and 900 °C, a short strengthening stage followed by a drop of flow stress and continuous softening were observed (Fig. 7). The drop of flow stress in the onset of straining could result from sporadic dislocations before plastic deformation or short-range order [21,54]. Meantime, further softening indicated the occurrence of dynamic recrystallisation (DRX) [54]. EBSD analysis showed that, in the bcc $Nb_{40}Ti_{40}V_{20}$ and weakly B2-ordered $Al_{15}Nb_{40}Ti_{40}V_5$ alloys deformed at 700 °C, bulging of initial grain boundaries was found (Fig. 8a, b). The formation of necklace microstructure, which is the signature of discontinuous DRX (DDRX), was observed in RH/MEAs deformed at relatively low temperatures and high strain rates [21,54–59]. In turn, in the highly B2-ordered $Al_{20}Nb_{40}Ti_{40}$ alloy, the microstructure was expectedly unchanged (Fig. 8c) because of the limited strain experienced by the sample (Table 4). Moreover, its fracture surface (insert in Fig. 8c) had the intergranular character, indicating the decreased grain boundary cohesion typical of ordered alloys and intermetallic compounds tested at high temperatures in the air [60,61].

DDRX persisted in the studied alloys deformed at 900 °C (Fig. 8d-f). This mechanism was dominant in the bcc $Nb_{40}Ti_{40}V_{20}$ and highly B2-ordered $Al_{20}Nb_{40}Ti_{40}$ alloys (Fig. 8d, f), while, in the weakly B2-ordered $Al_{15}Nb_{40}Ti_{40}V_5$ alloy, DDRX operated along with continuous DRX (CDRX) (Fig. 8e). The activation of CDRX in the $Al_{15}Nb_{40}Ti_{40}V_5$ alloy could be connected with its lower T_m compared to the $Nb_{40}Ti_{40}V_{20}$ and $Al_{20}Nb_{40}Ti_{40}$ alloys (Table 1), that is, with a higher homologous temperature of plastic deformation [21]. The co-operation of DDRX and CDRX resulted in the formation of a more homogeneous recrystallised microstructure in the $Al_{15}Nb_{40}Ti_{40}V_5$ alloy compared to the $Nb_{40}Ti_{40}V_{20}$ and $Al_{20}Nb_{40}Ti_{40}$ counterparts, containing a high fraction of initial unrecrystallised grains. Apparently, alleviated recrystallisation in the $Al_{15}Nb_{40}Ti_{40}V_5$ alloy ensured by simultaneous DDRX and CDRX lowered the stored elastic energy and refined the grains more effectively than sole DDRX did in the $Nb_{40}Ti_{40}V_{20}$ and $Al_{20}Nb_{40}Ti_{40}$ alloys, thereby promoting a ~ 76 % larger elongation (Fig. 7b; Table 4).

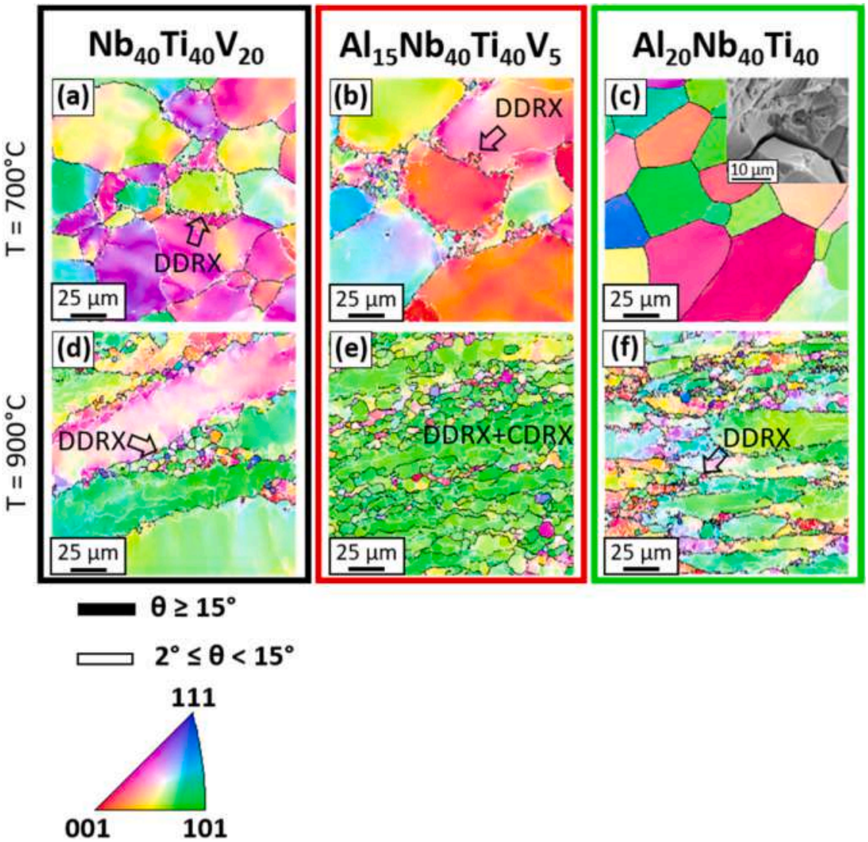

Fig. 8. Characterisation of the structure of the $Nb_{40}Ti_{40}V_{20}$, $Al_{15}Nb_{40}Ti_{40}V_5$, and $Al_{20}Nb_{40}Ti_{40}$ alloys after tensile tests at 700 and 900 °C: (a-c) IPF maps, showing the typical microstructures of the $Nb_{40}Ti_{40}V_{20}$ (a), $Al_{15}Nb_{40}Ti_{40}V_5$ (b), $Al_{20}Nb_{40}Ti_{40}$ (c) alloys after tensile tests at 700 °C; (d-f) IPF maps, showing the typical microstructures of the $Nb_{40}Ti_{40}V_{20}$ (a), $Al_{15}Nb_{40}Ti_{40}V_5$ (b), $Al_{20}Nb_{40}Ti_{40}$ (c) alloys after tensile tests at 900 °C. Black blank arrows in a, b, d, f denote microstructural features specific for DDRX. Insert in c displays the fracture surface of the $Al_{20}Nb_{40}Ti_{40}$ alloy after tensile test at 700 °C The tensile direction is horisontal.

4. Conclusions

In this study, the effect of Al-induced B2 ordering on the tensile mechanical properties of the $Al_xNb_{40}Ti_{40}V_{20-x}$ (x = 0; 15; 20 at%) RMEAs at 22–900 °C were investigated. The following conclusions can be made:

1) At 22 °C, Al had a minor effect on the tensile strength, increasing the yield strength from 650 to 795 MPa. Wherein, the weakly B2-ordered $Al_{15}Nb_{40}Ti_{40}V_5$ alloy achieved a higher uniform elongation compared to the bcc $Nb_{40}Ti_{40}V_{20}$ alloy, but the highly B2-ordered $Al_{20}Nb_{40}Ti_{40}$ counterpart was brittle. The microscopic localisation of plastic deformation, instead of macroscopic one in the bcc $Nb_{40}Ti_{40}V_{20}$ alloy, was assumed to ensure the improved ductility of the weakly B2-ordered $Al_{15}Nb_{40}Ti_{40}V_5$ alloy.
2) At 500 °C, all three alloys underwent a gradual softening, which was less pronounced in the highly B2-ordered $Al_{20}Nb_{40}Ti_{40}$ alloy. Both B2-ordered alloys remained stronger than the bcc $Nb_{40}Ti_{40}V_{20}$ alloy, and they manifested the PLC effect. The emergence of this effect was connected with the pinning-unpinning of dislocations by B2 domains.
3) At 700 °C, the bcc $Nb_{40}Ti_{40}V_{20}$ and weakly B2-ordered $Al_{15}Nb_{40}Ti_{40}V_5$ alloys softened drastically, while, in the highly B2-ordered $Al_{20}Nb_{40}Ti_{40}$ alloy, the strength reduction was minor. The superiority in the strength of the $Al_{20}Nb_{40}Ti_{40}$ alloy over the $Al_{15}Nb_{40}Ti_{40}V_5$ alloy was ascribed to the higher degree of B2 ordering, whereas its brittleness was explained by low grain boundary cohesion due to testing in the air. In the bcc $Nb_{40}Ti_{40}V_{20}$ and weakly B2-ordered $Al_{15}Nb_{40}Ti_{40}V_5$ alloys, the formation of necklace microstructure due to DDRX was observed.
4) At 900 °C, the B2-ordered alloys showed lower strength than the bcc $Nb_{40}Ti_{40}V_{20}$ alloy. Loss of strength in all the alloys was induced by the activation of diffusion-controlled dislocation climb/glide. In turn, the advantage from the B2 ordering was suggested to diminish due to disordering or decreasing degree of B2 ordering. In all three alloys, DDRX was active. But if in the bcc $Nb_{40}Ti_{40}V_{20}$ and highly B2-ordered $Al_{20}Nb_{40}Ti_{40}$ alloys, this mechanism was dominant, in the weakly B2-ordered $Al_{15}Nb_{40}Ti_{40}V_5$ alloy, it co-operated with CDRX. This DDRX+CDRX co-operation procured a more homogeneous recrystallised microstructure and effective reduction of stored energy, thereby providing over ~ 200 % of elongation in the weakly B2-ordered $Al_{15}Nb_{40}Ti_{40}V_5$ alloy.

CRediT authorship contribution statement

N. Yurchenko: Conceptualization, Validation, Formal analysis, Investigation, Data curation, Writing – original draft, Writing – review & editing, Visualization, Supervision, Project administration, Funding acquisition. **E. Panina:** Methodology, Investigation. **A. Tojibaev:** Methodology, Investigation. **V. Novikov:** Methodology, Investigation. **G. Salishchev:** Validation, Formal analysis, Data curation, Writing – review & editing, Supervision. **S. Zherebtsov:** Writing – review & editing, Supervision. **N. Stepanov:** Writing – review & editing, Supervision.

Data availability

Data will be made available on request.

Declaration of Competing Interest

The authors declare that they have no known competing financial interests or personal relationships that could have appeared to influence the work reported in this paper.

Acknowledgements

Funding: This work was supported by the Russian Science Foundation Grant no. 21-79-10043 (https://rscf.ru/en/project/21-79-10043/).

The work was carried out using the equipment of the Joint Research Center of Belgorod State National Research University "Technology and Materials" with financial support from the Ministry of Science and Higher Education of the Russian Federation within the framework of agreement No. № 075-15-2021-690 (unique identifier for the project RF----2296.61321×0030). The authors also thank Dr S. Mironov, Belgorod National Research University, for fruitful discussions, and Dr S. Naumov, Belgorod National Research University, for aid in preparing the ingots of the alloys.

Appendix A. Supporting information

Supplementary data associated with this article can be found in the online version at doi:10.1016/j.jallcom.2022.168465.

References

[1] O.N. Senkov, G.B. Wilks, D.B. Miracle, C.P. Chuang, P.K. Liaw, Refractory high-entropy alloys, Intermetallics 18 (2010) 1758–1765, https://doi.org/10.1016/j.intermet.2010.05.014
[2] O.N. Senkov, D.B. Miracle, K.J. Chaput, J.P. Couzinie, Development and exploration of refractory high entropy alloys - a review, J. Mater. Res. 33 (2018) 3092–3128, https://doi.org/10.1557/jmr.2018.153
[3] N.R. Philips, M. Carl, N.J. Cunningham, New opportunities in refractory alloys, Metall. Mater. Trans. A. (2020) 1–12, https://doi.org/10.1007/s11661-020-05803-3
[4] T. Li, Y. Lu, Z. Cao, T. Wang, T. Li, Opportunity and challenge of refractory high-entropy alloys in the field of reactor structural materials, Acta Met. Sin. 57 (2021) 42–54, https://doi.org/10.11900/0412.1961.2020.00293
[5] O.N. Senkov, G.B. Wilks, J.M. Scott, D.B. Miracle, Mechanical properties of Nb25Mo25Ta25W25 and V20Nb20Mo20Ta20W20 refractory high entropy alloys, Intermetallics 19 (2011) 698–706, https://doi.org/10.1016/j.intermet.2011.01.004
[6] K.-K. Tseng, C.-C. Juan, S. Tso, H.-C. Chen, C.-W. Tsai, J.-W. Yeh, Effects of Mo, Nb, Ta, Ti, and Zr on mechanical properties of equiatomic Hf-Mo-Nb-Ta-Ti-Zr alloys, Entropy 21 (2018) 15, https://doi.org/10.3390/e21010015
[7] S. Wu, D. Qiao, H. Zhang, J. Miao, H. Zhao, J. Wang, Y. Lu, T. Wang, T. Li, Microstructure and mechanical properties of CxHf0.25NbTaW0.5 refractory high-entropy alloys at room and high temperatures, J. Mater. Sci. Technol. 97 (2022) 229–238, https://doi.org/10.1016/J.JMST.2021.05.015
[8] T. Li, W. Jiao, J. Miao, Y. Lu, E. Guo, T. Wang, T. Li, P.K. Liaw, A novel ZrNbMoTaW refractory high-entropy alloy with in-situ forming heterogeneous structure, Mater. Sci. Eng. A 827 (2021) 142061, https://doi.org/10.1016/J.MSEA.2021.142061
[9] T. Li, J. Miao, Y. Lu, T. Wang, T. Li, Effect of Zr on the as-cast microstructure and mechanical properties of lightweight Ti2VNbMoZrx refractory high-entropy alloys, Int. J. Refract. Met. Hard Mater. 103 (2022) 105762, https://doi.org/10.1016/J.IJRMHM.2021.105762
[10] K.C. Lo, Y.J. Chang, H. Murakami, J.W. Yeh, A.C. Yeh, An oxidation resistant refractory high entropy alloy protected by CrTaO 4 -based oxide, Sci. Rep. 9 (2019) 1–12, https://doi.org/10.1038/s41598-019-43819-x
[11] B. Gorr, F. Müller, S. Schellert, H.-J. Christ, H. Chen, A. Kauffmann, M. Heilmaier, A new strategy to intrinsically protect refractory metal based alloys at ultra high temperatures, Corros. Sci. (2020) 108475, https://doi.org/10.1016/j.corsci.2020.108475
[12] Y.D. Wu, Y.H. Cai, T. Wang, J.J. Si, J. Zhu, Y.D. Wang, X.D. Hui, A refractory Hf25Nb25Ti25Zr25 high-entropy alloy with excellent structural stability and tensile properties, Mater. Lett. 130 (2014) 277–280, https://doi.org/10.1016/J.MATLET.2014.05.134
[13] N.Y. Yurchenko, N.D. Stepanov, A.O. Gridneva, M.V. Mishunin, G.A. Salishchev, S.V. Zherebtsov, Effect of Cr and Zr on phase stability of refractory Al-Cr-Nb-Ti-V-Zr high-entropy alloys, J. Alloy. Compd. (2018), https://doi.org/10.1016/j.jallcom.2018.05.099
[14] C. Frey, R. Silverstein, T.M. Pollock, A high stability B2-containing refractory multi-principal element alloy, Acta Mater. 229 (2022) 117767, https://doi.org/10.1016/J.ACTAMAT.2022.117767
[15] O.N. Senkov, D.B. Miracle, S.I. Rao, Correlations to improve room temperature ductility of refractory complex concentrated alloys, Mater. Sci. Eng. A 820 (2021) 141512, https://doi.org/10.1016/J.MSEA.2021.141512
[16] S.P. Wang, E. Ma, J. Xu, New ternary equi-atomic refractory medium-entropy alloys with tensile ductility: hafnium versus titanium into NbTa-based solution, Intermetallics 107 (2019) 15–23, https://doi.org/10.1016/j.intermet.2019.01.004
[17] S. Wei, S.J. Kim, J. Kang, Y. Zhang, Y. Zhang, T. Furuhara, E.S. Park, C.C. Tasan, Natural-mixing guided design of refractory high-entropy alloys with as-cast tensile ductility, Nat. Mater. 19 (2020) 1175–1181, https://doi.org/10.1038/s41563-020-0750-4
[18] Y. Chen, Z. Xu, M. Wang, Y. Li, C. Wu, Y. Yang, A single-phase V0.5Nb0.5ZrTi refractory high-entropy alloy with outstanding tensile properties, Mater. Sci. Eng. A 792 (2020) 139774, https://doi.org/10.1016/J.MSEA.2020.139774
[19] R.R. Eleti, N. Stepanov, N. Yurchenko, D. Klimenko, S. Zherebtsov, Plastic deformation of solid-solution strengthened Hf-Nb-Ta-Ti-Zr body-centered cubic medium/high-entropy alloys, Scr. Mater. 200 (2021) 113927, https://doi.org/10.1016/j.scriptamat.2021.113927
[20] A. Fu, Y. Cao, Y. Liu, S. Xu, Microstructure and mechanical properties of novel lightweight TaNbVTi-based refractory high entropy alloys, Materials 15 (2022) 355, https://doi.org/10.3390/MA15010355
[21] T. Li, Y. Lu, Z. Li, T. Wang, T. Li, Hot deformation behavior and microstructure evolution of non-equimolar Ti2ZrHfV0.5Ta0.2 refractory high-entropy alloy, Intermetallics 146 (2022) 107586, https://doi.org/10.1016/J.INTERMET.2022.107586
[22] L. Lilensten, J.-P. Couzinié, L. Perrière, A. Hocini, C. Keller, G. Dirras, I. Guillot, Study of a bcc multi-principal element alloy: tensile and simple shear properties and underlying deformation mechanisms, Acta Mater. 142 (2018) 131–141.
[23] O.N. Senkov, S.L. Semiatin, Microstructure and properties of a refractory high-entropy alloy after cold working, J. Alloy. Compd. 649 (2015) 1110–1123, https://doi.org/10.1016/j.jallcom.2015.07.209
[24] B. Schuh, B. Völker, J. Todt, N. Schell, L. Perrière, J. Li, J.P. Couzinié, A. Hohenwarter, Thermodynamic instability of a nanocrystalline, single-phase TiZrNbHfTa alloy and its impact on the mechanical properties, Acta Mater. 142 (2018) 201–212, https://doi.org/10.1016/J.ACTAMAT.2017.09.035
[25] C.H. Tu, S.K. Wu, C. Lin, A study on severely cold-rolled and intermediate temperature aged HfNbTiZr refractory high-entropy alloy, Intermetallics 126 (2020) 106935, https://doi.org/10.1016/j.intermet.2020.106935
[26] H. Huang, Y. Sun, P. Cao, Y. Wu, X. Liu, S. Jiang, H. Wang, Z. Lu, On cooling rates dependence of microstructure and mechanical properties of refractory high-entropy alloys HfTaTiZr and HfNbTiZr, Scr. Mater. 211 (2022) 114506, https://doi.org/10.1016/J.SCRIPTAMAT.2022.114506
[27] L. Lilensten, J.-P. Couzinié, J. Bourgon, L. Perrière, G. Dirras, F. Prima, I. Guillot, Design and tensile properties of a bcc Ti-rich high-entropy alloy with transformation-induced plasticity, Mater. Res. Lett. 5 (2017) 110–116, https://doi.org/10.1080/21663831.2016.1221861
[28] H. Huang, Y. Wu, J. He, H. Wang, X. Liu, K. An, W. Wu, Z. Lu, Phase-transformation ductilization of brittle high-entropy alloys via metastability engineering, Adv. Mater. 29 (2017) 1701678, https://doi.org/10.1002/adma.201701678
[29] R.R. Eleti, M. Klimova, M. Tikhonovsky, N. Stepanov, S. Zherebtsov, Exceptionally high strain-hardening and ductility due to transformation induced plasticity effect in Ti-rich high-entropy alloys, Sci. Rep. 10 (2020) 13293, https://doi.org/10.1038/s41598-020-70298-2
[30] T. dang Huang, S. yu Wu, H. Jiang, Y. ping Lu, T. min Wang, T. ju Li, Effect of Ti content on microstructure and properties of TixZrVNb refractory high-entropy alloys, Int. J. Miner. Metall. Mater. 27 (2020) 1318–1325, https://doi.org/10.1007/S12613-020-2040-1
[31] Z.Q. Xu, Z.L. Ma, Y. Tan, X.W. Cheng, Designing TiVNbTaSi refractory high-entropy alloys with ambient tensile ductility, Scr. Mater. 206 (2022) 114230, https://doi.org/10.1016/J.SCRIPTAMAT.2021.114230
[32] S. Zeng, Y. Zhou, H. Li, H. Zhang, H. Zhang, Z. Zhu, Microstructure and mechanical properties of lightweight Ti3Zr1.5NbVAlx (x = 0, 0.25, 0.5 and 0.75) refractory complex concentrated alloys, J. Mater. Sci. Technol. 130 (2022) 64–74, https://doi.org/10.1016/J.JMST.2022.05.005
[33] S. Zherebtsov, N. Yurchenko, E. Panina, M. Tikhonovsky, N. Stepanov, Gum-like mechanical behavior of a partially ordered Al5Nb24Ti40V5Zr26 high entropy alloy, Intermetallics 116 (2020) 106652, https://doi.org/10.1016/j.intermet.2019.106652
[34] S. Zherebtsov, N. Yurchenko, E. Panina, A. Tojibaev, M. Tikhonovsky, G. Salishchev, N. Stepanov, Microband-induced plasticity in a Ti-rich high-entropy alloy, J. Alloy. Compd. 842 (2020) 155868, https://doi.org/10.1016/j.jallcom.2020.155868
[35] L. Wang, S. Chen, B. li, T. Cao, B. Wang, L. Wang, Y. Ren, J. Liang, Y. Xue, Lightweight Zr1.2V0.8NbTixAly high-entropy alloys with high tensile strength and ductility, Mater. Sci. Eng. A 814 (2021) 141234, https://doi.org/10.1016/J.MSEA.2021.141234
[36] N. Yurchenko, E. Panina, A. Tojibaev, S. Zherebtsov, N. Stepanov, Overcoming the strength-ductility trade-off in refractory medium-entropy alloys via controlled B2 ordering, Mater. Res. Lett. 10 (2022) 813–823, https://doi.org/10.1080/21663831.2022.2109442/SUPPL_FILE/TMRL_A_2109442_SM6609.DOCX
[37] S.Y. Chen, L. Wang, W.D. Li, Y. Tong, K.K. Tseng, C.W. Tsai, J.W. Yeh, Y. Ren, W. Guo, J.D. Poplawsky, P.K. Liaw, Peierls barrier characteristic and anomalous strain hardening provoked by dynamic-strain-aging strengthening in a body-centered-cubic high-entropy alloy, Mater. Res. Lett. 7 (2019) 475–481, https://doi.org/10.1080/21663831.2019.1658233
[38] S. Chen, W. Li, F. Meng, Y. Tong, H. Zhang, K.K. Tseng, J.W. Yeh, Y. Ren, F. Xu, Z. Wu, P.K. Liaw, On temperature and strain-rate dependence of flow serration in

HfNbTaTiZr high-entropy alloy, Scr. Mater. 200 (2021) 113919, https://doi.org/10.1016/J.SCRIPTAMAT.2021.113919
[39] R.R. Eleti, N. Stepanov, N. Yurchenko, S. Zherebtsov, F. Maresca, Cross-kink unpinning controls the medium- to high-temperature strength of body-centered cubic NbTiZr medium-entropy alloy, Scr. Mater. 209 (2022) 114367, https://doi.org/10.1016/J.SCRIPTAMAT.2021.114367
[40] M. Wu, S. Wang, F. Xiao, G. Shen, Y. Tian, C. Yang, G. Zhu, D. Wang, D. Shu, B. Sun, Designing lightweight dual-phase refractory VNbTiSi-based eutectic high-entropy alloys for use at elevated temperatures, Mater. Sci. Eng. A 842 (2022) 143112, https://doi.org/10.1016/J.MSEA.2022.143112
[41] M. Wu, S. Wang, F. Xiao, G. Zhu, C. Yang, D. Shu, B. Sun, Dislocation glide and mechanical twinning in a ductile VNbTi medium entropy alloy, J. Mater. Sci. Technol. 110 (2022) 210–215, https://doi.org/10.1016/J.JMST.2021.09.016
[42] H. Chen, A. Kauffmann, S. Seils, T. Boll, C.H. Liebscher, I. Harding, K.S. Kumar, D.V. Szabó, S. Schlabach, S. Kauffmann-Weiss, F. Müller, B. Gorr, H.J. Christ, M. Heilmaier, Crystallographic ordering in a series of Al-containing refractory high entropy alloys Ta–Nb–Mo–Cr–Ti–Al, Acta Mater. 176 (2019) 123–133, https://doi.org/10.1016/j.actamat.2019.07.001
[43] S. Laube, H. Chen, A. Kauffmann, S. Schellert, F. Müller, B. Gorr, J. Müller, B. Butz, H.J. Christ, M. Heilmaier, Controlling crystallographic ordering in Mo–Cr–Ti–Al high entropy alloys to enhance ductility, J. Alloy. Compd. 823 (2020) 153805, https://doi.org/10.1016/j.jallcom.2020.153805
[44] D. Qiao, H. Liang, S. Wu, J. He, Z. Cao, Y. Lu, T. Li, The mechanical and oxidation properties of novel B2-ordered Ti2ZrHf0.5VNb0.5Alx refractory high-entropy alloys, Mater. Charact. 178 (2021) 111287, https://doi.org/10.1016/J.MATCHAR.2021.111287
[45] N.Y. Yurchenko, N.D. Stepanov, S.V. Zherebtsov, M.A. Tikhonovsky, G.A. Salishchev, Structure and mechanical properties of B2 ordered refractory AlNbTiVZrx (x = 0–1.5) high-entropy alloys, Mater. Sci. Eng. A 704 (2017) 82–90, https://doi.org/10.1016/j.msea.2017.08.019
[46] E. Passa, G. Shao, P. Tsakiropoulos, Beta phase decomposition in Nb-17 at% Al alloy, Philos. Mag. A Phys. Condens. Matter Struct.Defects Mech. Prop. 75 (1997) 637–655, https://doi.org/10.1080/01418619708207194
[47] T. Saito, T. Furuta, J.-H. Hwang, S. Kuramoto, K. Nishino, N. Suzuki, R. Chen, A. Yamada, K. Ito, Y. Seno, T. Nonaka, H. Ikehata, N. Nagasako, C. Iwamoto, Y. Ikuhara, T. Sakuma, Multifunctional alloys obtained via a dislocation-free plastic deformation mechanism, Science 300 (2003) 464–467, https://doi.org/10.1126/science.1081957
[48] M.J. Lai, C.C. Tasan, D. Raabe, Deformation mechanism of ω-enriched Ti–Nb-based gum metal: dislocation channeling and deformation induced ω–β transformation, Acta Mater. 100 (2015) 290–300, https://doi.org/10.1016/J.ACTAMAT.2015.08.047
[49] S. Zherebtsov, N. Yurchenko, D. Shaysultanov, M. Tikhonovsky, G. Salishchev, N. Stepanov, Microstructure and mechanical properties evolution in HfNbTaTiZr refractory high entropy alloy during cold rolling, Adv. Eng. Mater. (2020), https://doi.org/10.1002/adem.202000105
[50] S. Wang, M. Wu, D. Shu, B. Sun, Kinking in a refractory TiZrHfNb0.7 medium-entropy alloy, Mater. Lett. 264 (2020) 127369, https://doi.org/10.1016/j.matlet.2020.127369
[51] T.S. Rong, Serrated yielding in the B2-ordered Nb–15Al–20V alloy, Intermetallics 11 (2003) 151–155, https://doi.org/10.1016/S0966-9795(02)00196-6
[52] O.N. Senkov, S. Gorsse, D.B. Miracle, High temperature strength of refractory complex concentrated alloys, Acta Mater. 175 (2019) 394–405, https://doi.org/10.1016/J.ACTAMAT.2019.06.032
[53] N.S. Stoloff, R.G. Davies, The plastic deformation of ordered FeCo and Fe3Al alloys, Acta Mater. 12 (1964) 473–485, https://doi.org/10.1016/0001-6160(64)90019-7
[54] R.R. Eleti, T. Bhattacharjee, A. Shibata, N. Tsuji, Unique deformation behavior and microstructure evolution in high temperature processing of HfNbTaTiZr refractory high entropy alloy, Acta Mater. 171 (2019) 132–145, https://doi.org/10.1016/j.actamat.2019.04.018
[55] R.R. Eleti, A.H. Chokshi, A. Shibata, N. Tsuji, Unique high-temperature deformation dominated by grain boundary sliding in heterogeneous necklace structure formed by dynamic recrystallization in HfNbTaTiZr BCC refractory high entropy alloy, Acta Mater. 183 (2020) 64–77, https://doi.org/10.1016/J.ACTAMAT.2019.11.001
[56] F. Dong, Y. Yuan, W. Li, Y. Zhang, P.K. Liaw, X. Yuan, H. Huang, Hot deformation behavior and processing maps of an equiatomic MoNbHfZrTi refractory high entropy alloy, Intermetallics 126 (2020) 106921, https://doi.org/10.1016/j.intermet.2020.106921
[57] Z.C. Bai, X.F. Ding, Q. Hu, M. Yang, Z.T. Fan, X.W. Liu, Unique deformation behavior and microstructure evolution in high-temperature processing of a low-density TiAlVNb2 refractory high-entropy alloy, J. Alloy. Compd. (2021) 160962, https://doi.org/10.1016/j.jallcom.2021.160962
[58] T. Cao, W. Guo, W. Lu, Y. Xue, W. Lu, J. Su, C.H. Liebscher, C. Li, G. Dehm, Strain rate dependent deformation behavior of BCC-structured Ti29Zr24Nb23Hf24 high entropy alloy at elevated temperatures, J. Alloy. Compd. 891 (2022) 161859, https://doi.org/10.1016/J.JALLCOM.2021.161859
[59] Z. Yu, B. Xie, Z. Zhu, B. Xu, M. Sun, High-temperature deformation behavior and processing maps of a novel AlNbTi3VZr1.5 refractory high entropy alloy, J. Alloy. Compd. 912 (2022) 165220, https://doi.org/10.1016/J.JALLCOM.2022.165220
[60] C.T. Liu, C.L. White, Dynamic embrittlement of boron-doped Ni3Al alloys at 600°C, Acta Met. 35 (1987) 643–649, https://doi.org/10.1016/0001-6160(87)90187-8
[61] V.K. Sikka, E.A. Loria, Characteristics of a multicomponent Nb–Ti–Al alloy via industrial-scale practice, Mater. Sci. Eng. A 239–240 (1997) 745–751, https://doi.org/10.1016/S0921-5093(97)00662-X